

Pterodactyl: Guidance and Control of a Symmetric Deployable Entry Vehicle using an Aerodynamic Control System

Benjamin W. L. Margolis*, Wendy A. Okolo[†], and Sarah N. D’Souza[‡]
NASA Ames Research Center, Moffett Field, CA 94035, USA

Breanna J. Johnson[§]
NASA Johnson Space Center, Houston, TX 77058, USA

The NASA-funded Pterodactyl project seeks to advance the current state-of-the-art for entry vehicles by developing novel guidance and control technologies for Deployable Entry Vehicles (DEVs). This paper presents the guidance and control design and analysis for a mechanically-deployed DEV with a symmetric aeroshell and aerodynamic control surfaces. We present guidance tuning using both bank angle modulation with the Fully-Numerical Predictor Corrector Entry Guidance technique (FNPEG) and angle of attack and sideslip modulation with FNPEG with uncoupled range control (FNPEG URC). We show the control system design and simulation results for tracking both types of guidance commands.

I. Introduction

THE need for precision landing of high mass payloads on Mars or returning sensitive samples from other planetary bodies to specific locations on Earth is driving the development of an innovative NASA technology called a Deployable Entry Vehicle (DEV). Traditional entry vehicles for high mass missions do not scale well for launch vehicles currently available, driving the need for this innovative solution. NASA’s Space Technology Mission Directorate (STMD) has invested in two types of DEVs: i) the Adaptable, Deployable, Entry Placement Technology (ADEPT, [1, 2]) and ii) a Hypersonic Inflatable Aerodynamic Decelerator (HIAD, [3]). As part of the development of these DEV technologies, new thermal protection system (TPS) materials have been developed and manufactured to enable a flexible TPS for stowage. Additionally, the underlying deployment mechanisms have been successfully integrated with the flexible TPS to demonstrate successful deployment of the TPS.

The primary design challenge remaining for DEVs is the integration of a guidance and control (G&C) system that meets precision targeting requirements. The current state-of-the-art for entry control systems like Mars Science Laboratory is rooted in heritage entry, descent, and landing (EDL) systems such as Apollo. These rigid entry vehicles use Reaction Control System (RCS) thrusters, installed within the backshell, to achieve the desired bank command profile [4]. DEVs are radically different from rigid entry vehicles because DEVs have no backshell, which is the typical location for installation of RCS thrusters and associated fuel lines. Aerodynamic control systems, such as flaps, are being investigated as an effective means of entry precision targeting for DEVs. Aerodynamic control systems rely on direct modulation of aerodynamic forces, as opposed to modulating propulsive forces, to change the attitude of the vehicle. These systems have the potential to improve targeting, save propellant mass, or save payload volume as shown in Figure 1.

In a previously published work, NASA’s Pterodactyl project established a feasible mechanical design for integrating a flap control system with a mechanically deployed, asymmetric ADEPT DEV called the Pterodactyl Baseline Vehicle I (PBV-I) [5]. The feasibility of PBV-I was demonstrated in its ability to track a bank guidance trajectory to target the terminal descent initiation point for a lunar sample return mission to Earth. The flap control system allocated more payload volume and provided increased maneuverability, depending on dynamic pressure, compared to an analogous propulsive, bank control system. Challenges to the integrated PBV-I configuration were also identified. It was found that due to the asymmetry of the aeroshell, PBV-I was not able to track an angle of attack and sideslip (α/β) guidance profile [6, 7]. Additionally, due to the asymmetry of the aeroshell and the high speed entry, challenges arose with high heating on the edge of the flaps and stowing the DEV [8, 9]. Given the gains in payload volume and targeting performance

*Research Aerospace Engineer, Systems Analysis Office, MS 258-1, AIAA Member

[†]Aerospace Research Engineer, Intelligent Systems Division, MS 269-1, AIAA Member

[‡]Principal Investigator, Systems Analysis Office, MS 258-1, AIAA Member

[§]Aerospace Engineer, Flight Mechanics and Trajectory Design Branch, EG5, AIAA Member

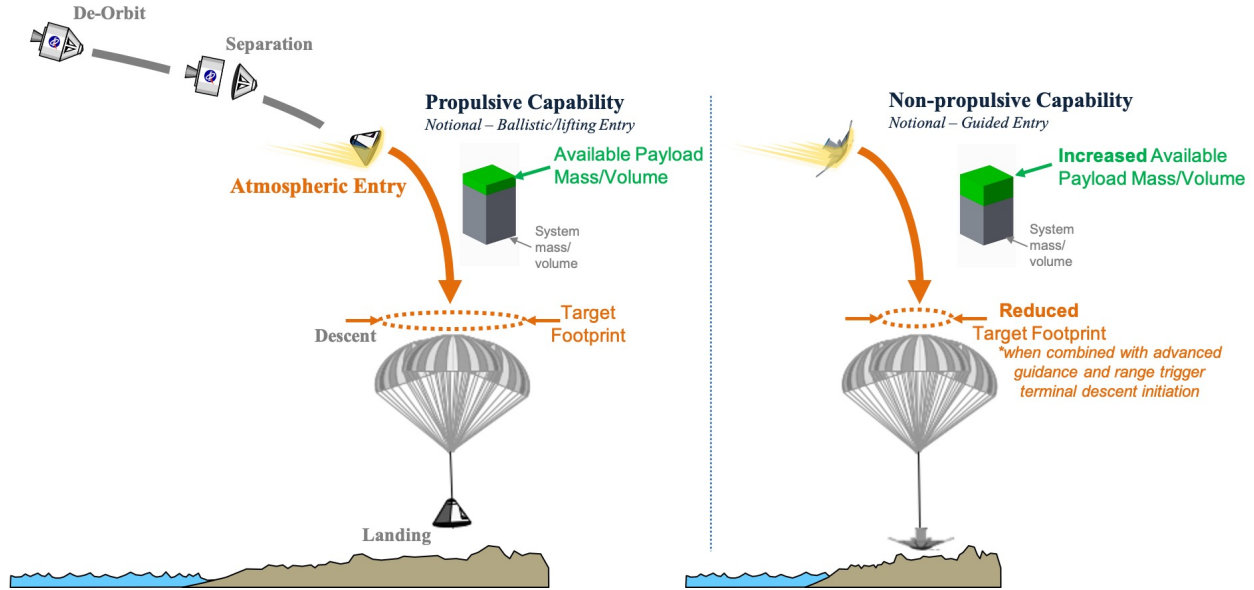


Figure 1 Concept of operations for the current propulsive heritage approach compared to that of a non-propulsive control system. Demonstrating the potential gain in mass and volume and improved targeting.

provided by the flap control system, this paper focuses on an alternative configuration to address some of the challenges with PBV-I.

The research discussed in this paper builds on the PBV-I work to characterize the capability of a scaled up, symmetric DEV, called PBV-II, integrated with a flap control system to perform the same lunar sample return mission to Earth. In this paper, we present the development and analysis of guidance and control techniques for the new vehicle. The paper is organized as follows. First we will describe the mission and vehicle configuration. Next, we present the control system design and controllable angle of attack and sideslip envelope. Next, we present guidance algorithm tuning and trajectory analysis. Finally, we present simulation results for the controlled vehicle.

II. Mission and Vehicle Overview

A. Lunar Return Mission

The scope of the flap control analysis is applied only to the entry phase of EDL operations, where the entry phase terminates at the descent initiation point. Therefore, the flap control system is designed to steer the vehicle while it decelerates from an entry speed of 11 km/s, to a Mach number of 2 at a latitude and longitude corresponding to the target location, Utah Test and Training Range (UTTR), as shown in Figure 2. The Mach 2 condition was selected based on past studies [10] and missions that use a similar descent initiation point. A lunar return mission was selected because the high Earth entry speeds will stress the integrated system with flaps due to the need to manage high aerodynamic loads and heat rates. A heat rate limit of 250 W/cm^2 was identified based on the ADEPT material limit determined through Arc-jet testing at NASA Ames Research Center [11]. The g-load limit was set at 15 g's, based on past missions and studies for returning non-biological or biological samples to Earth that are sensitive to deceleration loads [12–17].

B. PBV-II and Aerodynamic Control Surface Architecture

The Pterodactyl project selected a modified asymmetric version of ADEPT as the initial baseline configuration for its entry control system studies because a majority of the subsystems and mechanical design had been established [18]. This configuration had the added benefit of being a rigid structure, providing numerous potential mounting locations for the control effectors. The initial Pterodactyl Baseline Vehicle without entry control systems is shown in Figure 3. The layout of the vehicle with numbered flaps is shown in Figure 4(a) with stowage constraints shown in Figure 4(b). The longitudinal flaps (1, 2, 7, and 8) are designed to provide primarily pitch control by changing the vehicle's

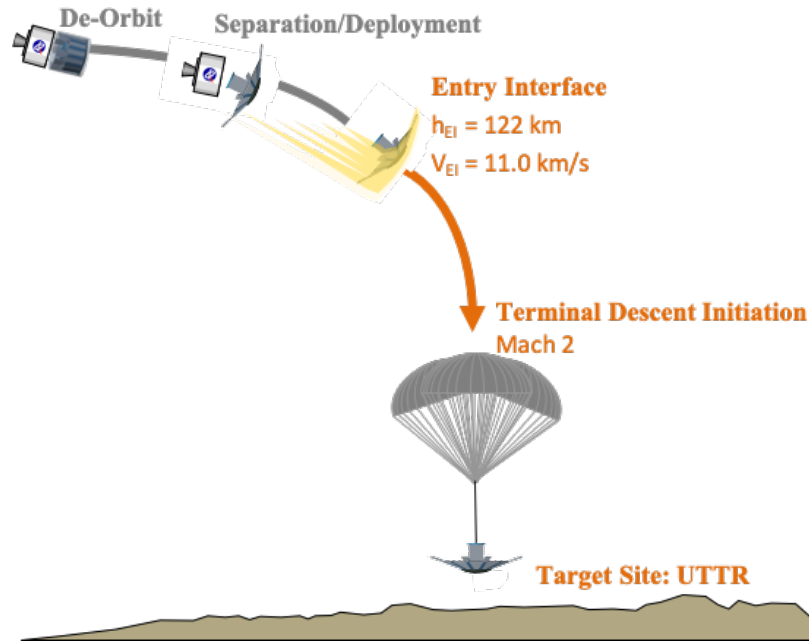


Figure 2 Lunar sample return concept of operations used for flap control system analysis.

angle of attack while the lateral flaps (3 - 6) are designed primarily for yaw control to modulate the sideslip. Deflecting longitudinal flaps 1 and 2 into the flow generates a negative/downwards pitch moment while doing the same for flaps 7 and 8 generates a positive/upwards pitch moment. When deflected into the flow, flaps 3 and 4 yaw the vehicle right (starboard) while flaps 5 and 6 create a yaw left (port) orientation. All flaps have a maximum of 20° deflection into the flow (+20°) and 45° retraction (-45°) out of the flow due to in-flight aerothermal limits and mechanical design integration constraints, respectively [8, 9].

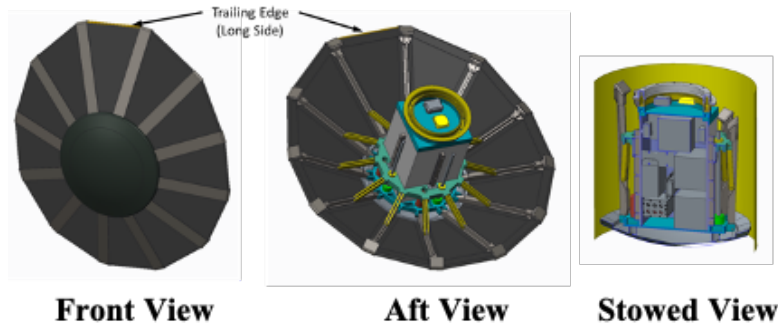


Figure 3 Pterodactyl Baseline Vehicle I (asymmetric, without control systems)

Initially, the Pterodactyl project studied and developed three different control system options for the PBV-I and assessed the performance of each option. The three options that were evaluated were flaps, center of mass shifting via mass movement, and propulsive reaction control system, included to provide a baseline. Given the payload volume savings and the increased maneuverability, the project team and stakeholders selected a flap control system for further study [5]. The flap configuration from the first round of trade studies, designated as PBV-I for this paper is shown in Figure 4.

To address the challenges encountered for PBV-I, the PBV aeroshell was made symmetric and scaled up to 2.86 m diameter, while keeping the ballistic coefficient in the same family as that of PBV-I. Scaling up the vehicle was needed due to the ADEPT TPS fabric thickness required to handle the heat load that results from lunar return entry conditions [8]. It was found that the dynamics of the asymmetric aeroshell of PBV-I resulted in a relatively high trim

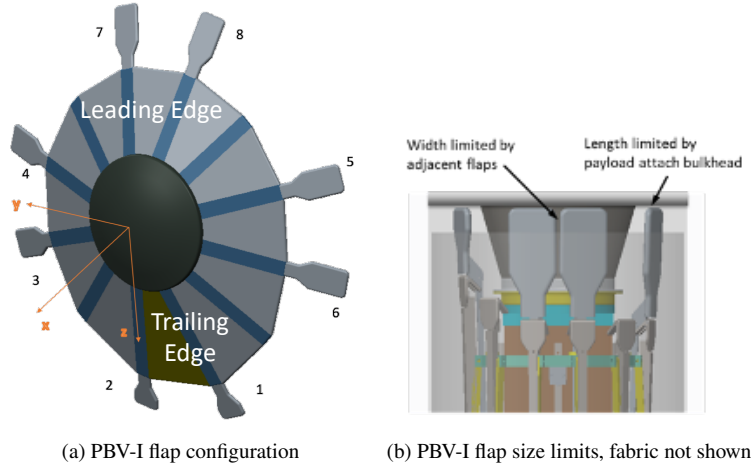


Figure 4 PBV-I

angle of attack, $\alpha_{trim} = -14^\circ$, causing increased heating on the flap edges and overwhelmed flap control authority when tracking α/β guidance commands to meet precision targeting requirements. Thus, the aeroshell was made symmetric to determine its effect on the flap control system design and performance. The scaled-up, symmetric flaps control configuration is designated as PBV-II in this paper and shown in Figure 5. The flap numbering scheme was preserved. We also note that although the vehicle exhibits one-eighth symmetry geometrically, due to the definition of angle of attack and sideslip as Euler angle rotations the symmetry is only about the $\alpha = 0$ and $\beta = 0$ lines.

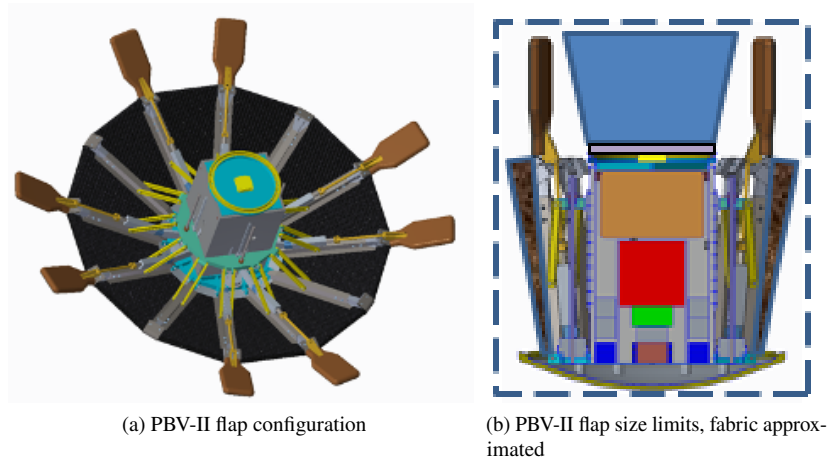


Figure 5 PBV-II

III. Methodology

The guidance and control analysis followed a process similar to the one employed during the PBV-I control system trade study [5, 7]. First, preliminary controls analysis was performed to ensure that consistent model data was being used, to assess stability of the vehicle, and to provide performance constraints for guidance algorithms, as described in Section IV. After the initial controls assessment, the parameters for the guidance algorithm were tuned and a baseline guidance profile was identified that provided satisfactory performance in a Monte Carlo simulation, as described in Section V. Finally, another set of control system analysis is performed for tracking the guidance reference profile, as presented in Section VI.

IV. Control System Design

A. Equations of Motion

The translational dynamics ignoring planet rotation are given by

$$\begin{aligned}\dot{V} &= -\frac{g(z)}{m} \sin(\gamma) - \frac{1}{m}D \\ \dot{\gamma} &= \left(-\frac{g(z)}{mV} + \frac{V}{z}\right) \cos(\gamma) \\ &\quad + \frac{1}{mV} (L \cos(\sigma) - S \sin(\sigma)) \\ \dot{\xi} &= \frac{1}{mV \cos(\gamma)} (L \sin(\sigma) + S \cos(\sigma))\end{aligned}$$

where V is the velocity of the vehicle, γ is the vehicle flight-path angle, ξ is the vehicle heading angle defined from due North, L , D , and S are the aerodynamic lift, drag, and side forces, respectively, $g(z)$ is the force due to gravity, dependent on the radial distance from the planet center z , σ is the bank angle, and m is the mass of the vehicle.

The angular dynamics are given by

$$\begin{bmatrix} \dot{p} \\ \dot{q} \\ \dot{r} \end{bmatrix} = \left(\mathbb{I}_b^{B/B_{cm}}\right)^{-1} \left(\begin{bmatrix} \mathcal{L} \\ \mathcal{M} \\ \mathcal{N} \end{bmatrix} - \begin{bmatrix} p \\ q \\ r \end{bmatrix} \times \mathbb{I}_b^{B/B_{cm}} \begin{bmatrix} p \\ q \\ r \end{bmatrix} \right)$$

where p , q , and r are the angular velocities about the body-fixed x , y , and z axes respectively, $\mathbb{I}_b^{B/B_{cm}}$ is the inertia tensor of the vehicle about its center of mass expressed in the body coordinates and \mathcal{L} , \mathcal{M} , and \mathcal{N} are the aerodynamic roll, pitch, and yaw moments, respectively.

The angular kinematics are defined by

$$\begin{aligned}\dot{\sigma} &= p \cos(\alpha) \sec(\beta) + r \sin(\alpha) \sec(\beta) \\ \dot{\alpha} &= -p \cos(\alpha) \tan(\beta) + q - r \sin(\alpha) \tan(\beta) \\ \dot{\beta} &= p \sin(\alpha) - r \cos(\alpha)\end{aligned}$$

where α is the angle of attack and β is the sideslip angle. Finally, the translational kinematics are given by

$$\begin{aligned}\dot{z} &= V \sin(\gamma) \\ \dot{\Phi} &= \frac{V}{z} \cos(\gamma) \cos(\xi) \\ \dot{\lambda} &= \frac{V}{z \cos(\Phi)} \cos(\gamma) \sin(\xi)\end{aligned}$$

where Φ and λ are the latitude and longitude of the vehicle center of mass.

The aerodynamic forces and moments are dependent on the angle of attack and sideslip as well as the Mach number M and control surface deflections $\delta_1, \dots, \delta_8$ as defined above. These aerodynamic forces and moments are of the form

$$F = \bar{q} S_A C_{(\cdot)}(\alpha, \beta, M, \delta_1, \dots, \delta_8) \quad (1)$$

and

$$T = \bar{q} S_A \bar{c} C_{(\cdot)}(\alpha, \beta, M, \delta_1, \dots, \delta_8) \quad (2)$$

respectively, where $C_{(\cdot)}$ are the dimensionless aerodynamic force and moment coefficients, S_A is the reference surface area, \bar{c} is a reference length, \bar{q} is the dynamic pressure defined by

$$\bar{q} = \frac{1}{2} \rho V^2$$

with ρ the altitude-dependent atmospheric density. The aerodynamic coefficients in (1) and (2) are determined by interpolating the aerodynamic database developed in [19] using spline basis functions [20].

B. LQR Control design for angle of attack and sideslip control

The vehicle state used for the attitude simulation is modeled as

$$x = [p \ q \ r \ \sigma \ \alpha \ \beta \ e_\sigma \ e_\alpha \ e_\beta]^T$$

where e_σ , e_α , and e_β are the augmented integral error state variables. The control input is modeled as

$$u = [\delta_1 \ \delta_2 \ \dots \ \delta_8]^T$$

where each δ_i is the deflection of the i th flap with $\delta_i = 0$ parallel to the rib, positive deflections indicating deflection into the flow and negative deflection indicating movement out of the flow.

To develop the linear controller, we linearize the equations of motion, for the states defined above, at the desired point in the flight envelope to obtain state-space linear equations of the form

$$\Delta \dot{x} = A \Delta x + B \Delta u$$

where Δx and Δu are deviations from the linearization point x^* , u^* . The matrices A and B defined by

$$A = \left. \frac{\partial f}{\partial x} \right|_{x^*, u^*} \quad B = \left. \frac{\partial f}{\partial u} \right|_{x^*, u^*}$$

are called the state and input matrices respectively. Here, $f(x, u)$ is the vector-valued function of the derivatives for each state variable concatenated together.

The linearization point is chosen by assuming steady-state conditions, no integral error, symmetric nominal control surface deflections, and trim angle of attack from a Newton-Raphson solver. The control system is designed at the flight conditions where the 3 degree-of-freedom guidance simulation indicates activation of the guidance and control. This leads to the conditions listed in Table 1. The control law is given by

$$u = u^* - K \Delta x$$

where K is the feedback gain matrix. The feedback gain K is computed to minimize the quadratic cost function

$$J = \int_0^\infty \Delta x^T(\tau) Q \Delta x(\tau) + \Delta u^T(\tau) R \Delta u(\tau) d\tau$$

and can be found using a number of numerically stable algorithms by constructing the appropriate Algebraic Riccati Equation or Linear Matrix Inequality [21]. The Q and R matrices are diagonal weighting matrices for the states and control surfaces respectively. These matrices are tuned by evaluating the simulation and selecting the Q and R element values that provide desirable performance and control effort usage. The values for all elements on R were the same, given by $R_{ii} = 5 \times 10^{-6}$. The Q matrix is given by

$$Q = \text{diag}([22.8 \ 22.8 \ 22.8 \ 91.2 \ 91.2 \ 91.2 \ 91.2 \ 91.2 \ 91.2])$$

where the diag operator constructs a diagonal matrix where the elements on the diagonal are given by the arguments.

C. Angle of Attack and Sideslip Control Envelope

In order to track the angle of attack and sideslip commands from the guidance algorithm, the control system must be able to hold the commanded attitude during flight. However, the range of angle of attack and sideslip commands that the vehicle can actually maintain is determined by the vehicle geometry, control actuators, and control algorithm. In this section, we present the process for determining the control envelope – the range of holdable angle of attack and sideslip that the controlled vehicle could achieve if commanded.

To determine the control envelope, a sweep of 1600 step-response simulations was performed. For each simulation, the state was initialized at the nominal trim configuration. The vehicle is commanded to hold this trim for fifty seconds, at which point the vehicle is commanded to a particular angle of attack α_c and sideslip β_c . All simulations were performed at a constant Mach of 40 and dynamic pressure of 200 Pascals corresponding to the flight conditions of guidance and control activation for the lunar return mission. The angle of attack and sideslip commands ranged from 0

Table 1 Linearization point for control system design

Variable	Values
Mach number, M	39
dynamic pressure, \bar{q} Pa	345
angular velocity, p^* , q^* , r^* , deg/s	0
sideslip angle β^* , deg	0
bank angle σ^* , deg	0
control surface deflection δ_i^* , deg	-30
angle of attack α^* , deg	0
integral error, e_σ^* , e_α^* , e_β^* , deg·s	0

to 20 degrees in 0.5 degree increments. Due to the vehicle's quarter symmetry in angle of attack and sideslip, only commands with non-negative angle of attack and sideslip are evaluated.

Next, the response to each command was evaluated using the final state of the controlled vehicle. We use the sum of the square magnitude of the attitude error and angular velocity, denoted by

$$d^2(\alpha_c, \beta_c) = \sigma_f^2 + (\alpha_f - \alpha_c)^2 + (\beta_f - \beta_c)^2 + p_f^2 + q_f^2 + r_f^2$$

where the f subscript indicates the final value of the controlled vehicle in response to the step response command of α_c and β_c . Since the commanded bank angle and angular velocity are zero, this performance metric corresponds to the square magnitude of the error in state space. Using the d^2 metric we categorize the final attitude as trimmable or not. To do this, we define the holdable set as

$$X_h = \{(\alpha_f, \beta_f) \mid d^2(\alpha_c, \beta_c) \leq \tau\}$$

which is a threshold criteria on the d^2 metric. In Figure 6, we show a representation of the step responses performed in the envelope study by projecting the commanded and final values onto the angle of attack and sideslip plane. Commanded attitudes are indicated with black + symbols, final attitudes in the holdable set are shown with a green × symbol while final attitudes not in the holdable set are shown with an orange × symbol.

We can visually inspect Figure 6 to identify the control envelope under nominal conditions. When either the angle of attack or angle of sideslip is zero, the envelope extends out to 19.0 degrees magnitude. When the angle of attack and sideslip are equal, the envelope extends to about 15 degrees in angle of attack and sideslip. Note that these lines correspond to the one-eighth symmetry of the vehicle and that off these lines of symmetry the control envelope does not extend as far. Additionally, there are uncontrollable regions for the vehicle just off the $\alpha = 0$ and $\beta = 0$ lines.

The uncontrollable regions are likely due to the roll moments generated by the control surfaces when deflected. Trimming these induced roll moments reduces the control authority for pitch and yaw moment trimming and thus reduces the range of the controllable α/β envelope. This contrasts the analysis of the PBV-I [7], where the reduction in control authority came from the base aeroshell inducing roll moments that the flaps needed to overcome to hold a particular attitude. Figure 7 shows the step responses for two similar attitude commands of $\alpha_c = 4.0$, $\beta_c = 12.0$ in blue and $\alpha_c = 1.5$, $\beta_c = 13.0$ in orange with the commands shown in dashed lines of the appropriate colors. If the roll on the flaps were not a significant factor, we would expect the flaps 5 and 6 to deflect into the flow and flaps 3 and 4 to deflect out of the flow to yaw left and flaps 7 and 8 to deflect into the flow and flaps 1 and 2 to retract out of the flow to pitch up. Indeed, all the flaps begin moving in those expected directions. However, for both responses multiple flaps change course to counter the induced roll which causes the bank to immediately deviate. The controller attempts to counter the induced roll at the expense of tracking the angle of attack and sideslip. This controller's success in the attitude maneuver depends on the dynamic behavior finding an appropriate trim condition fast enough that it does not roll out of control. The controller does successfully find the trim conditions for the $\alpha_c = 4.0$, $\beta_c = 12.0$ case but not the $\alpha_c = 1.5$, $\beta_c = 13.0$ case. For the latter case, the controller puts the control surfaces into a pinwheel-like configuration, alternating flaps into and out of the flow to generate a roll moment to bring the bank angle back to zero. For the former case, the controller reduces the deflection of flap 5 and moves flaps 7 and 2 in the opposite direction from the expected direction to control the roll.

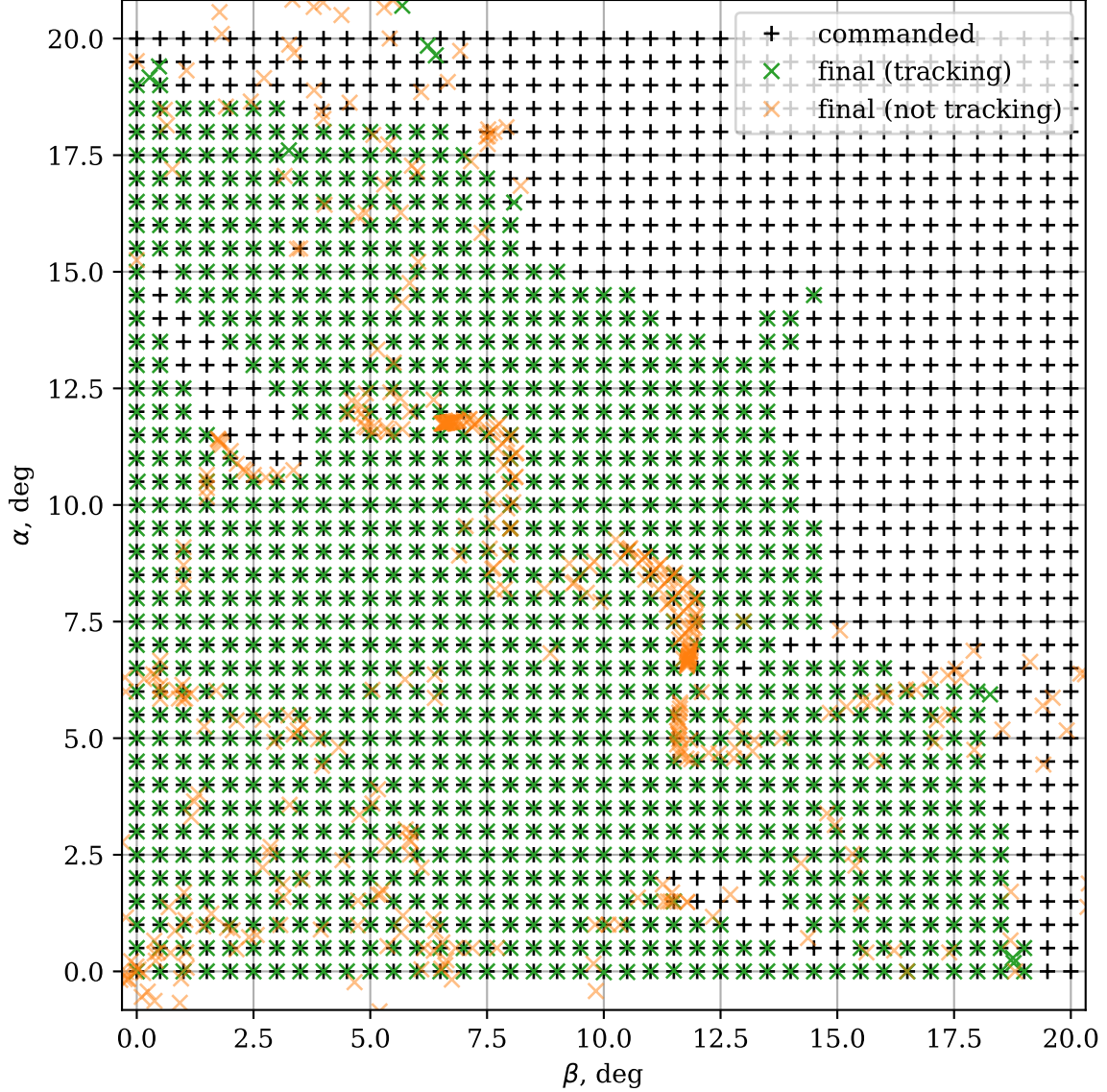


Figure 6 Control envelope visualization

The angle of attack and sideslip guidance algorithm can be parameterized by angle of attack and sideslip limits so that the algorithm only generates attitude commands that can be achieved. Since these limits are encoded as box constraints, that is each variable is bounded by a lower and upper limit independently, values of ± 10 degrees were used as limits for both angle of attack and sideslip. These values were chosen to ensure that any attitude in the box constraint could be achieved with a controllability margin to account for control envelope variation with flight condition and to preserve some control authority to reject disturbances.

D. LQR Control design for Yaw-to-Bank Architecture

A novel yaw-to-bank architecture was developed for the PBV-I to leverage its dihedral effect to achieve high performance bank control. In this approach, the control design is decomposed into an inner and outer loop. The outer control loop tracks bank angle commands by commanding the appropriate sideslip that induces a roll moment through the dihedral effect [7]. The inner control loop tracks (i) angle of attack commands from guidance including regulation about a constant angle of attack and (ii) sideslip commands generated by the outer control loop. A block diagram of the architecture is shown in Figure 8. Note that the inner loop does not need to regulate angle of attack if the system design

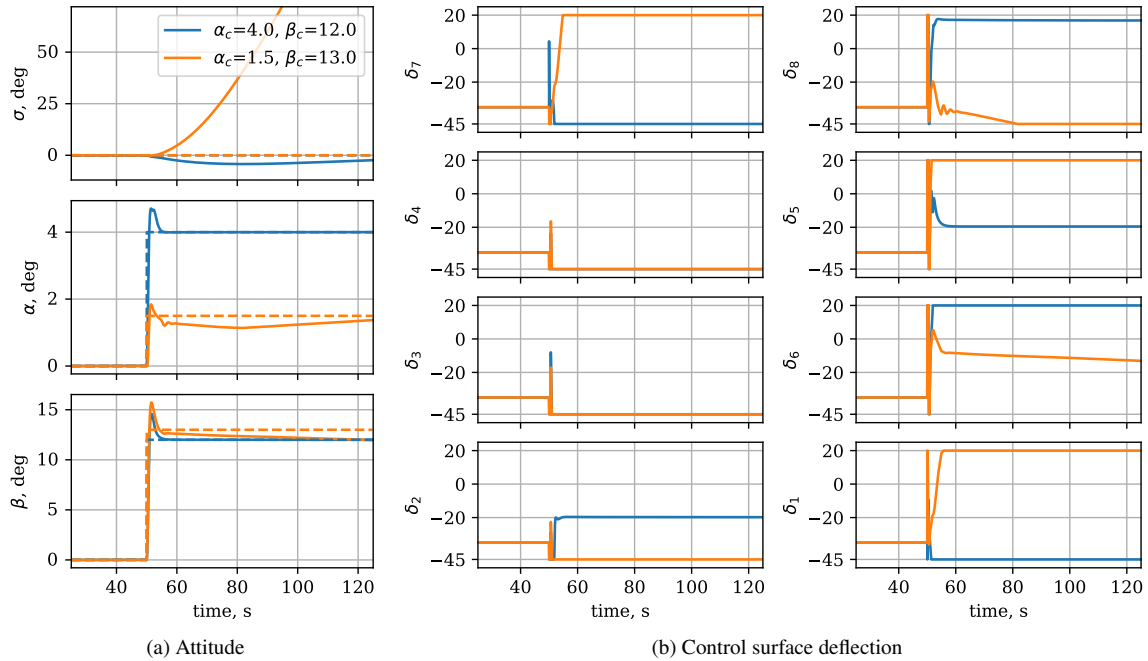


Figure 7 Step response for two angle of attack and sideslip commands used to find control envelope

does not require it, such as for a longitudinally stable entry vehicle.

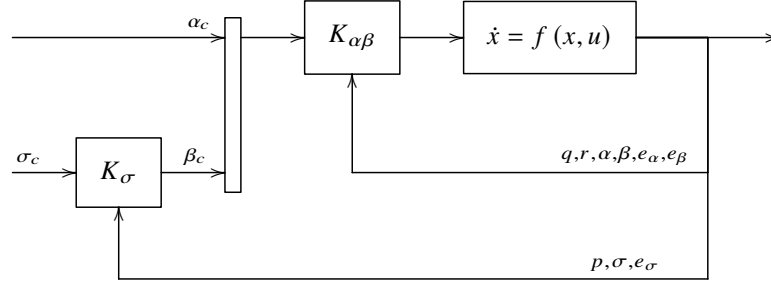


Figure 8 Block diagram of bank control system innovation

Unlike the PBV-I, the PBV-II is capable of holding sufficiently large angle of attack and sideslip commands making a guidance method based on those commands feasible. However, a PBV-II variant called PBV-IIa with a CG offset was modeled to assess the yaw-to-bank control architecture using aerodynamic control surfaces on a DEV with a symmetric aeroshell. The PBV-IIa was designed with a CG offset to provide the same trim angle of attack as PBV-I. The control system was re-implemented for this new vehicle with minimal manual tuning of the Q and R weighting matrices from the PBV-I.

V. Guidance and Trajectory Analysis

For PBV-I, a guidance algorithm was developed for vehicles with stronger pitch and yaw control authority, leveraging the core principles of the Fully Numerical Predictor-corrector Entry Guidance (FNPEG) [6, 22, 23]. The augmented guidance, FNPEG for Uncoupled Range Control (FNPEG URC), was used in PBV-II development to assess trajectory performance and generate trajectory design maps. FNPEG URC was used to generate the angle of attack and sideslip angle (α/β) commands that augment the vehicle's total lift and drag vectors to steer the vehicle to the targeted position and energy state. This methodology differs from FNPEG which generates bank angle (σ) commands to instead roll the

vehicle’s total lift vector, steering the vehicle to the target.

Similar to the work done for PBV-I [6], the focus of the PBV-II trajectory studies is to understand the feasibility of a lunar return mission and the general capability of the vehicle. Numerical predictor-correctors were chosen for this study due to their flexibility in adapting to varied input conditions in Entry Interface (EI) state, target state, and vehicle attributes. Unlike the heritage entry guidance flown on the Apollo missions, numerical predictor correctors like FNPEG do not necessitate the definition of a reference trajectory to generate the sets of linearized feedback gains that would then be used to generate commands in flight. This was an important advantage of using this class of algorithms, ensuring that despite changes in vehicle configuration and aerodynamics data from PBV-I to PBV-II, very little to no tuning was required to achieve similar levels of success. Additionally, this particular numerical predictor was chosen due to its capability to perform both skip and direct entries [22, 23]. For the trajectories generated in this study, the fact that these two classes of entry problems are handled internally is a useful feature, since many feasible EI states exist for high speed (11 km/s) lunar return trajectories but can result in direct, lofted, or even skip entry profiles [22, 23].

Feasibility was assessed based on the key performance parameters of peak heat rate, peak g-load, and target miss distance upon guidance termination. The PBV-II had constraints imposed, dictating that no trajectory encounters peak heating greater than 250 W/cm^2 , g-loads greater than $15 \text{ g}'s$, or miss distances greater than 3 km.

For guidance analysis, the control system actuation was emulated with an angle of attack rate and acceleration limiter at $5^\circ/s$ and $5^\circ/s^2$ respectively. Sideslip rate and acceleration were also limited to $5^\circ/s$ and $5^\circ/s^2$. The integration rate and simulated dynamics were modeled at 100 Hz with guidance called at a slower rate of 1 Hz. All trajectory profiles shown used the Earth Global Reference Atmospheric Model (GRAM) 2010 and an 8x8 Lagrangian gravity field. Trajectories were run according to the mission concept of operations (ConOps) input parameters defined in Table 2 and target the Utah Testing and Training Range (UTTR) [6, 24] at a 31 km altitude, marking the end of entry and the beginning of descent system initiation. The EI parameters of flight path angle, latitude, and longitude were unrestrained and allowed to vary between simulation runs. While PBV-II was originally developed for an α/β guided mission, sub-Sections V.A-V.C detail the trajectory analysis of PBV-II using both FNPEG URC and FNPEG methods.

Table 2 EI and guidance target parameters.

EI Parameters	Value	Guidance Target Parameters	Value
Altitude	122 km	Altitude of Target Energy	31 km
Relative Velocity	11 km/s	Relative Velocity of Target Energy	0.69 km/s
Relative Azimuth	0°	Latitude Target	40°
		Longitude Target	-112°

A. Gain Tuning Effects on Trajectory Performance

While a new guidance profile was needed for each change in vehicle mass, surface area, and reference aerodynamics, there was no need to tune the guidance algorithm parameters to achieve success. Trajectory design maps with parametric sweeps of EI states were created for PBV-II and are detailed in [25]. From that analysis, similar performance was observed between symmetric and asymmetric aerodynamics, FNPEG and FNPEG URC, and PBV-I and PBV-II. Because of this, another trajectory analysis was performed to determine how changes in guidance tuning parameters could yield even more desirable performance.

Both FNPEG and FNPEG URC rely on a user-defined control angle at a target energy to define an angle profile that is linear with respect to energy. This angle profile is used within the predictor-corrector throughout flight [6]. The target bank angle for FNPEG is designated σ_F and the target angle of attack for FNPEG URC is designated α_F . Figure 9(a) shows that the altitude profiles for the different gains tested are nearly identical for most of the trajectory despite the use of different guidance schemes. All trajectories use the same EI and target conditions, meeting all the needed constraints. These altitude profiles begin to diverge after peak dynamic pressure (400 seconds) based on the chosen final angle tuning parameter. As expected, a smaller σ_F corresponds with a trajectory that terminates with more lofting due to the smaller bank angle which corresponds to a lift vector pointed more in the zenith direction. This is also highlighted in Figure 9b, where the $\sigma_F = 30^\circ$ corresponds with the most lofted trajectory tail and $\sigma_F = 90^\circ$ corresponds with the steepest. Similarly, Figure 9c shows that a more negative α_F , giving more lift pointed in the zenith direction, corresponds to the FNPEG URC trajectories terminating with more loft. For both guidances, the final few seconds of

flight deviate from their linear angle vs. energy profiles to clean up any over or undershoot. These guidance parameters have little effect on the sideslip profile, shown in Figure 9d. Note that in both bank and α - β cases, the downrange to target is 3400km while the typical crossrange incurred ranges between 10 to 30 km for the six cases shown in Figure 9e. While the 3D projection of the position shows larger crossrange incursions for FNPEG, it should be noted that for this trajectory, trim angle of attack is at a relatively higher magnitude (-14°) as compared to the angles of attack explored by FNPEG URC ($\pm 10^\circ$). Since these are all starting at the same EI with the same initial energy to be expended, any excess energy is dispensed into the crossrange channel, ensuring severe overshoot or undershoot of the target does not occur. It should be noted that a more preferable EI longitude may be non-coincident with the target (-112°), but was held constant to aid in the comparison of the FNPEG and FNPEG URC guidances.

Since the symmetric PBV-II performed well across multiple tuning parameters for trajectories under nominal conditions, a qualitative evaluation of the compared nominal trajectories was needed to determine the best α_F for PBV-II. While all FNPEG URC cases shown in Figure 9 reached some unfavorable saturation in the sideslip channel for nominal trajectories, only the $\alpha_F=8^\circ$ tuned trajectory reached angle of attack saturation, leaving $\alpha_F=4^\circ$ and $\alpha_F=-8^\circ$ as possible candidates. Since this is a high speed lunar return trajectory, some loft, and thus regimes of low dynamic pressure are expected between the two dynamic pressure peaks that occur before and after the altitude "hill" shown at 250 seconds in Figure 9(a). However, since the vehicle's control system relies on aerodynamic pressure for effective control, these regimes have the possibility of introducing periods of little to no control authority. This is undesirable, as any propulsive maneuvers during entry are to be avoided if possible. For this reason, $\alpha_F=4^\circ$ was chosen to conservatively preserve lift margin and control authority for any future stress cases that the vehicle may encounter. This gain was also used to perform Monte Carlo trades in the determination of a baseline nominal trajectory.

B. PBV-II Baseline Selection

While FNPEG URC does not generate commands based on a reference trajectory like other heritage entry guidances, the definition of a baseline trajectory that performs well under nominal and off-nominal conditions is still useful to define the expected performance envelope of the vehicle. Similar to the methodology used for PBV-I [6], a scan of EI latitude, longitude, and flight path angle (FPA) combinations were used to determine this baseline, with all other nominal EI conditions held constant. Figure 10 shows the results of this EI sweep, where each asterisk represents a 1,000 case Monte Carlo run with the dispersions typical for a lunar return trajectory as shown in Table 3. Earth GRAM dispersions were applied by dispersing the random number seed, nr1, uniformly between 1 and 30,000. The aerodynamic coefficients were also uniformly dispersed.

Table 3 Monte Carlo inputs.

Monte Carlo Variables	Standard Deviation	Monte Carlo Variables	Multiplier
Initial Altitude	± 0.1 km	C_L, C_D, C_S	0.9-1.1
Initial Velocity	± 3.33 m/s		
Initial Mass	$\pm 1\%$ kg		
Initial Azimuth	$\pm 0.1^\circ$		
Initial Latitude	$\pm 0.1^\circ$		
Initial Longitude	$\pm 0.1^\circ$		

For FNPEG URC, each flight path angle had multiple points yielding mean miss distances below 3 km, Chapman Aerothermal heat rates well below 250 W/cm², and g-loads below 15 g's. Figures 10(a)-(c) show that a baseline trajectory, selected for the most desirable performance, would lie between EI states 2,000 - 4,000 km upstream of the target. EI states within 2,000 km of the target result in excessive heat rates while EI states greater than 4,000 km from the target would yield cases that exceed the 3 km constraint. Lastly, Figure 10(d) shows that a smaller magnitude flight path angle corresponds with a desired higher minimum dynamic pressure between the two peaks of the dynamic pressure curve as well as decreased peak dynamic pressure. However, $\gamma=-5.1^\circ$ lies close to the flight path angle that would yield in skip out [24]. Thus, $\gamma=-5.2^\circ$ was selected for the baseline. A minimum dynamic pressure of 500 Pa in nominal and off-nominal trajectories was selected as a desired trajectory attribute, helping to further define the baseline trajectory to 2,800 km (where all flight path angles yield a minimum dynamic pressure of >500 Pa). This dynamic pressure

was chosen as an indicator signifying that there is likely enough appreciable atmosphere for a control system to be effective throughout nominal and off-nominal flight. The range to target of 2,800 km was also preferable in the amount of crossrange incurred as compared to the previously chosen baseline of 3,400 km for PBV-I [6]. Figure 11 shows that with this update, the amount of sideslip angle needed to reduce this crossrange is also reduced, resulting in a baseline nominal trajectory with no saturation. Resulting final energy states at the target are shown in Figure 12 for this baseline.

C. Guidance Comparison at Selected Entry Interface

While analysis showed that an α/β trajectory in the face of dispersions was feasible for PBV-II, bank angle guidance using the yaw-to-bank control architecture [7] was also evaluated for the symmetric aeroshell. The PBV-IIa vehicle variant with a CG offset has the same trim angle of attack as PBV-I. This angle of attack facilitates comparisons PBV-I bank trajectories as well as comparison between bank and α/β trajectories for PBV-II.

Using the same EI conditions as the baseline from Table 2 and dispersions from Table 3, similar miss distances were observed between the two guidance methods. Figure 13 shows similar FNPEG performance to the results of the FNPEG URC case from Figure 12 in miss distance at the targeted energy state. These results agree with those from previous results [6] suggesting that, like for PBV-I, bank angle and α/β guidances can produce very similar performance before CG, rolling, pitching, and yawing uncertainties are introduced into the trajectory tradespace. These kinds of dispersions were not applied in this 3-degree of freedom (3-DOF) simulation and should be fully explored in future 6-DOF analyses. If there is enough control authority to overcome those dispersions and both are begun at favorable EI states, both guidance methods have the ability to yield satisfactory performance.

VI. Tracking Results and Discussion

In this section, we present the simulation results for attitude control of the PBV-II in the angle of attack and sideslip control configuration and the yaw-to-bank control configuration.

A. Angle of Attack and Sideslip Tracking Results

In this section, we discuss the simulation results for the control system described in Section IV.B tracking the guidance profile presented in Section V.B. Figure 14(a) shows the controller tracks the commanded angle of attack and sideslip well throughout the flight under nominal conditions. During rapid maneuvers in angle of attack or sideslip, such as occur at 50 and 225 seconds, there are deviations in bank angle but the magnitude is kept below 0.1 degrees.

Figure 14(b) shows the control surface deflections throughout the flight. Until guidance activation around twenty seconds, the control surfaces are held at their trim -30 degree deflection. When the guidance algorithm begins issuing commands to the controller, the control surfaces are moved rapidly to track the initial rapid slews. Note that the controller must move the flaps to counter the roll moment generated by the flaps themselves and cannot simply use the longitudinal flaps to trim the pitch moment and lateral flaps to trim the yaw moment to hold a particular attitude, as discussed in Section IV.C.

B. Bank Angle Command Tracking Results

In this section, we discuss the simulation results for the control system described in Section IV.B tracking the guidance profile presented in Section V.B. Figure 15(a) shows that the controller tracks the commanded bank angle well throughout the flight under nominal conditions. During rapid bank maneuvers, such as the first slew around 120 seconds, the bank reversal at 350 seconds, and the final slew shortly thereafter, there are sharp deviations in sideslip angle to accelerate the bank angle in the appropriate direction by inducing a roll moment via the dihedral effect. Since the yaw-to-bank control architecture leverages the inherent stability of the vehicle to hold a trim attitude and needs relatively little sideslip to induce sufficient roll, the flap motion shown in Figure 15(b) is quite small.

VII. Conclusion and Future Work

In this paper, we presented the guidance and control development and analysis of the Pterodactyl project's PBV-II. Using FNPEG and FNPEG URC, feasible guidance profiles were developed using both angle of attack and sideslip commands and bank angle commands. Using a standard LQR controller architecture with feedback gains designed using linearized dynamics, we developed a control system using aerodynamic actuators that could hold any angle of attack and sideslip attitude in a control envelope of ± 10 degrees in each angle and track the corresponding guidance profile

with those constraints. Using the novel yaw-to-bank control architecture, we developed a control system that could track bank angle commands. Future work could study the guidance and controls results in a fully integrated six-degree of freedom simulation environment to assess performance. The G&C development could also benefit from an analysis of the robustness to dispersions. In a companion paper [25] some dispersion robustness capability is presented but further dispersion analysis would enhance our understanding of the capability of this vehicle configuration.

The biggest determining factor in comparing these guidance methods is the selected control system authority and whether the vehicle can feasibly achieve the angles commanded in flight. The largest challenge for employing α/β in an actual flight will depend on the static and dynamic aerodynamic moment uncertainties, center of mass uncertainties, and general ability to maintain the desired bank angle of zero throughout flight. While the results in Sections V.B are promising, true feasibility of the guidance would rely on how well the vehicle can recover from any roll disturbances, as the desired bank angle of 0° is not a physical stability point like the trim alpha and beta natural stability points exploited for bank angle trajectories. If there is enough control authority to overcome those dispersions and both are begun at favorable EI states, both guidance methods have the ability to yield satisfactory performance. Both bank angle and α/β guidance methods can produce very similar performance before CG, rolling, pitching, and yawing uncertainties are introduced into the trajectory tradespace. These dispersions were not applied in either guidance or control system simulations and should be fully explored in future integrated simulation. Both approaches show promise for precision targeting for hypersonic entry vehicles.

Acknowledgments

The authors acknowledge the support of the Pterodactyl aerodynamicist, Brandon Reddish, and the mechanical design lead, Bryan Yount, for their data, insight, and contributions to the body of work presented in this paper. The authors would also like to acknowledge the support of the NASA Space Technology Mission Directorate (STMD) Early Career Initiative Program Manager, Ricky Howard, the NASA STMD Entry Descent & Landing Principal Technologist, Michelle Munk, and all internal and external Pterodactyl mentors, especially Jeffrey Barton of the Johns Hopkins Applied Physics Laboratory, who supported this effort and provided valuable feedback and recommendations.

References

- [1] Venkatapathy, E., Hamm, K., Fernandez, I., Arnold, J., Kinney, D., Laub, B., Makino, A., McGuire, M., Peterson, K., Prabhu, D., Empey, D., Dupzyk, I., Huynh, L., Hajela, P., Gage, P., Howard, A., and Andrews, D., "Adaptive Deployable Entry and Placement Technology (ADEPT): A Feasibility Study for Human Missions to Mars," *21st AIAA Aerodynamic Decelerator Systems Technology Conference and Seminar*, AIAA 2011-2608, Dublin, Ireland, 2011.
- [2] NASA/Space Technology Mission Directorate, "Adaptable, Deployable, Entry, and Placement Technology (ADEPT SR-1)," , 2018. URL <https://gameon.nasa.gov/adept-sr-1/>, date: 23.01.2018.
- [3] NASA/Space Technology Mission Directorate, "Hypersonic Inflatable Aerodynamic Decelerator," , 2014. URL https://www.nasa.gov/directorates/spacetech/game_changing_development/HIAD/index.html, date: 05.06.2014.
- [4] D'Souza, S. N., and Sarigul-Klijn, N., "Survey of Planetary Entry Guidance Algorithms," *Journal of Progress in Aerospace Sciences*, Vol. 68, 2014, pp. 64–74.
- [5] Alunni, A. I., D'Souza, S. N., C., B., Okolo, W. A., Nikaido, B. E., Margolis, B. W., Johnson, B. J., Barton, J. D., Lopez, G., Wolfarth, L. S., and Hays, Z. B., "Pterodactyl: Trade Study for an Integrated Control System Design of a Mechanically Deployable Entry Vehicle," *AIAA SciTech 2020 Forum*, AIAA, Orlando, FL, 2020.
- [6] Johnson, B. J., Rocca-Bejar, D., Lu, P., Nikaido, B. E., Yount, B. C., D'Souza, S. N., and Hays, Z. B., "Pterodactyl: Development and Performance of Guidance Algorithms for a Mechanically Deployed Entry Vehicle," *AIAA SciTech 2020 Forum*, AIAA, Orlando, FL, 2020.
- [7] Okolo, W. A., Margolis, B. W., D'Souza, S. N., and Barton, J. D., "Pterodactyl: Development and Comparison of Control Architectures for a Mechanically Deployed Entry Vehicle," *AIAA SciTech 2020 Forum*, AIAA, Orlando, FL, 2020.
- [8] Yount, B. C., Cassell, A. M., and D'Souza, S. N., "Pterodactyl: Mechanical Designs for Integrated Control Design of a Mechanically Deployed Entry Vehicle (DEV)," *AIAA SciTech 2020 Forum*, AIAA, Orlando, FL, 2020.
- [9] Hays, Z. B., Yount, B. C., Nikaido, B. E., Tran, J., D'Souza, S. N., Kinney, D. J., and McGuire, M. K., "Pterodactyl: Thermal Protection System for Integrated Control Design of a Mechanically Deployed Entry Vehicle," *AIAA SciTech 2020 Forum*, AIAA, Orlando, FL, 2020.

- [10] Cianciolo, A. M., Davis, J. L., Engelund, W., Komar, D. R., and Queen, E., "Entry, Descent, and Landing Systems Analysis Study: Phase 2 Report on Exploration Feed-Forward Systems," *NASA Technical Manual*, , No. 217055, February 2011.
- [11] Cassell, A., Smith, B., Wercinski, P., Ghassemieh, S., Hibbard, K., Nelessen, A., and Cutts, J., "ADEPT, A Mechanically Deployable Re-Entry Vehicle System, Enabling Interplanetary CubeSat and Small Satellite Missions," *32nd Annual AIAA/USU Conference on Small Satellites*, SSC18-XII-18, Utah, 2018.
- [12] Tindol, R., "NASA: Genesis Sample Return," *Press Kit*, September 2004.
- [13] SERRANO-MARTINEZ, J., and HECHLER, M., "Aerocapture guidance and navigation for the Rosetta Comet Nucleus Sample Return Mission," *Guidance, Navigation, and Control and Co-located Conferences*, AIAA 89-3381, 1989.
- [14] Ceglia, E., *European Users Guide to Low Gravity Platforms, Chapter 6*, European Space Agency, 2005.
- [15] Mitcheltree, R., Kellas, S., Dorsey, J., Desai, P., and Martin, C., "A passive Earth-entry capsule for Mars Sample Return," *7th AIAA/ASME Joint Thermophysics and Heat Transfer Conference*, AIAA 98-2851, 1998.
- [16] Gooding, J. L., "Scientific Guidelines for Preservation of Samples Collected from Mars," *NASA Technical Memorandum*, , No. 4148, April 1990.
- [17] Veverka, J., "Cryogenic Comet Nucleus Sample Return (CNSR) Mission Technology Study," *NASA SDO Report*, 2010.
- [18] Directorate, N. S. T. M., "Center Innovation Fund 2016 Winners Nano-ADEPT Lifting: Design Development for a Lifting Flight Test Demonstration," , 2016. URL <https://www.nasa.gov/centers/ames/cct/office/cif/p-Wercinski>.
- [19] Reddish, B. J., Nikaido, B. E., D'Souza, S. N., Hawke, V., and Kang, H., "Pterodactyl: Aerodynamic Modeling for a Symmetric Deployable Earth Entry Vehicle with Flaps," *AIAA SciTech 2021 Forum*, AIAA, 2021.
- [20] W. L. Margolis, B., and Lyons, K., "ndsplines: A Python Library for Tensor-Product B-Splines of Arbitrary Dimension," *Journal of Open Source Software*, Vol. 4, No. 42, 2019, p. 1745. doi:10.21105/joss.01745, URL <http://dx.doi.org/10.21105/joss.01745>.
- [21] Boyd, S., El Ghaoui, L., Feron, E., and Balakrishnan, V., *Linear matrix inequalities in system and control theory*, Vol. 15, Siam, 1994.
- [22] Lu, P., Brunner, C. W., Stachowiak, S. J., Mendeck, G. F., Tigges, M. A., and Cerimele, C. J., "Verification of a fully numerical entry guidance algorithm," *Journal of Guidance, Control, and Dynamics*, Vol. 40, No. 2, 2017, pp. 230–247.
- [23] Lu, P., "Entry guidance: a unified method," *Journal of Guidance, Control, and Dynamics*, Vol. 37, No. 3, 2014, pp. 713–728.
- [24] D'Souza, S. N., Okolo, W. A., Nikaido, B. E., Yount, B. C., Tran, J., Margolis, B. W., Smith, B., Cassell, A. M., Johnson, B. J., Hibbard, K., Barton, J. D., and Hays, Z. B., "Developing an Entry Guidance and Control Design Capability Using Flaps for the Lifting Nano-ADEPT," *AIAA Aviation 2019 Forum*, AIAA, Dallas, TX, 2019.
- [25] D'Souza, S. N., Alunni, A. I., Yount, B., Okolo, W. A., Margolis, B. W., Johnson, B. J., Rocca-Bejar, D., Hibbard, K. E., Barton, J. D., Hawke, V., Hays, Z. B., and Reddish, B., "Pterodactyl: System Analysis of an Asymmetric and Symmetric Deployable Entry Vehicle for Precision Targeting Using Flaps," *AIAA SciTech 2021 Forum*, AIAA, 2021.

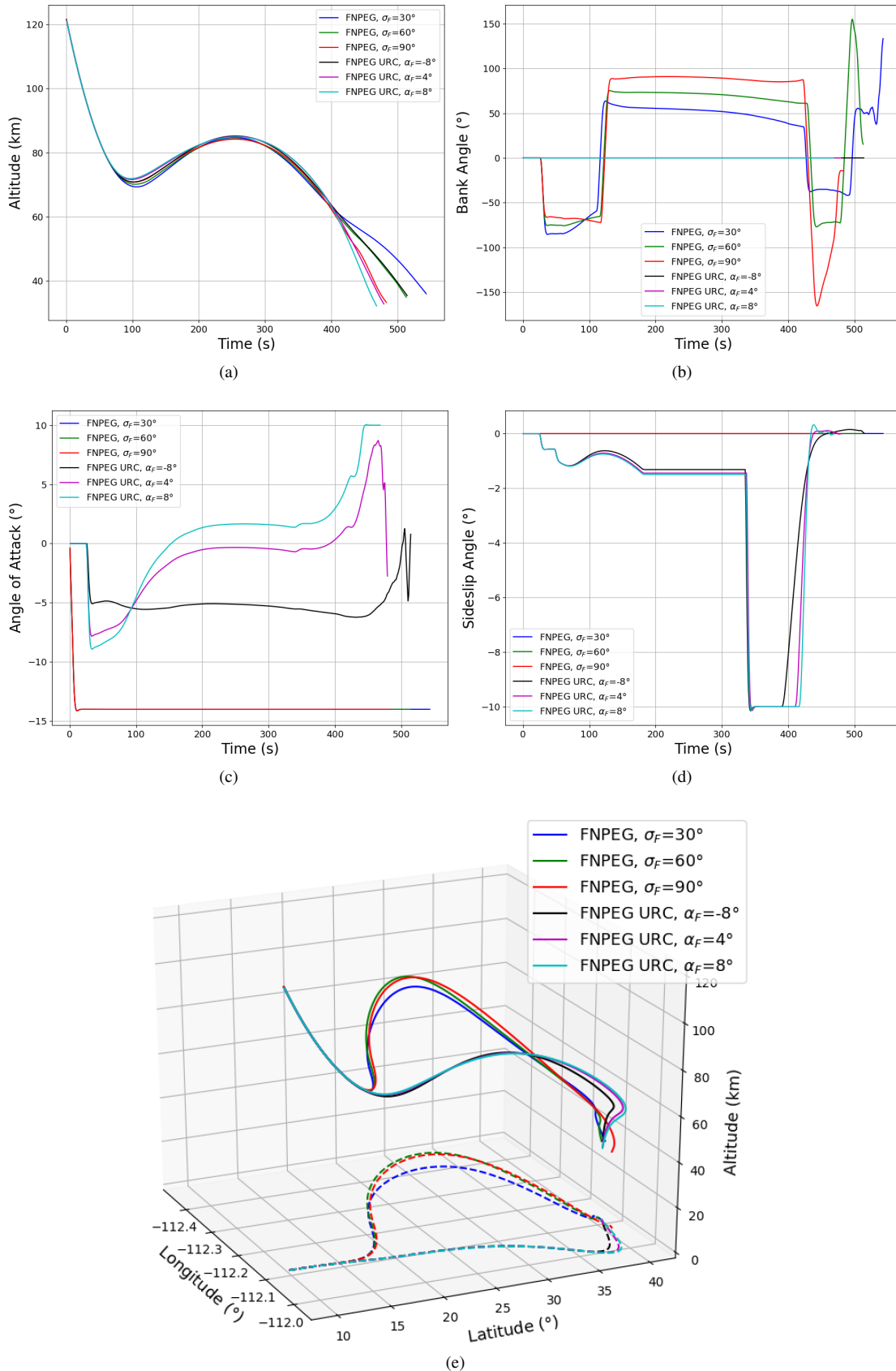


Figure 9 Guidance Tuning Parameter Effects on Trajectory Profiles: a) Altitude; b) Bank Angle; c) Angle of Attack; d) Sideslip Angle; e) Position.

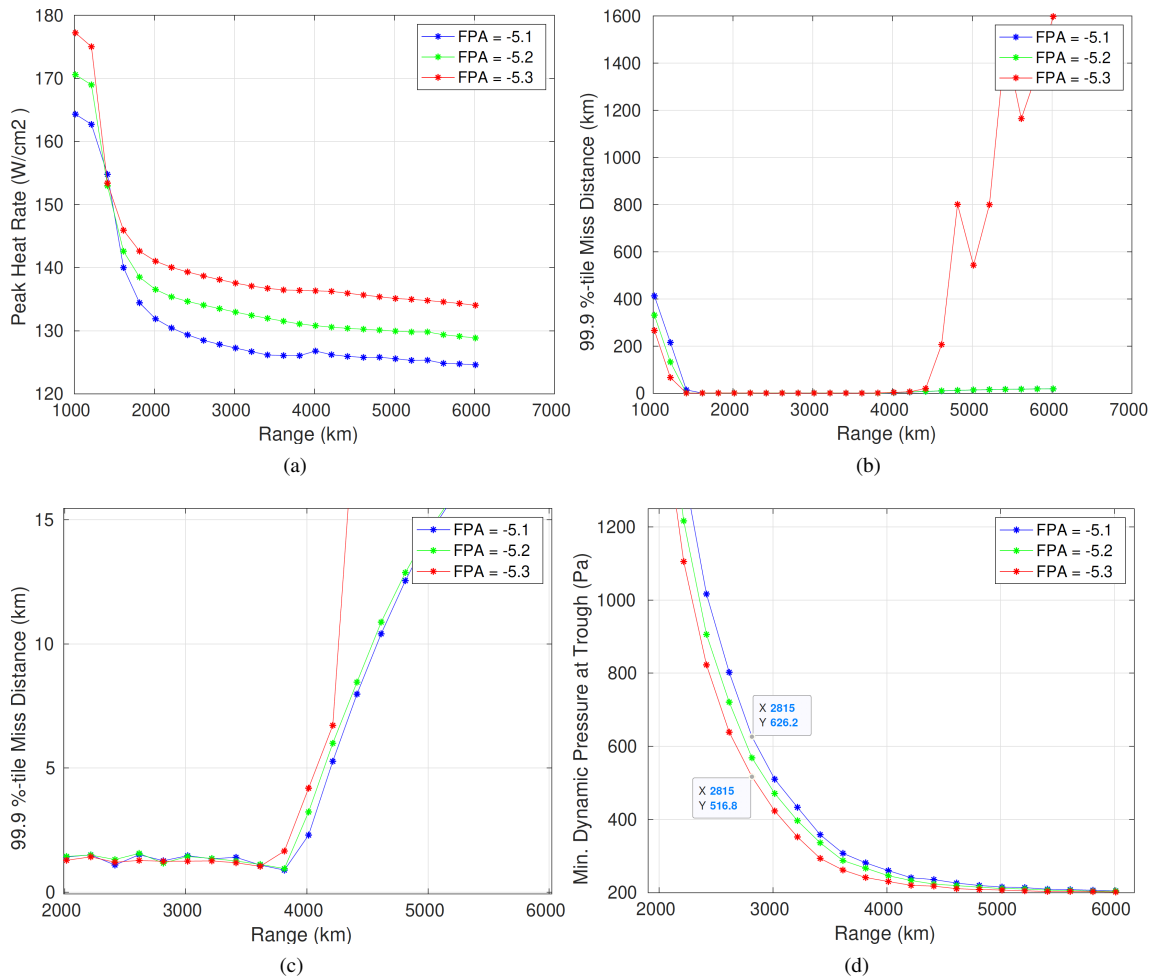


Figure 10 FNPEG URC EI Selection Effect on Key Performance Parameters: a) Peak Heat Rate; b) 99.9 Percentile Miss Distance; c) 99.9 Percentile Miss Distance (magnified); d) Minimum Dynamic Pressure at Trough

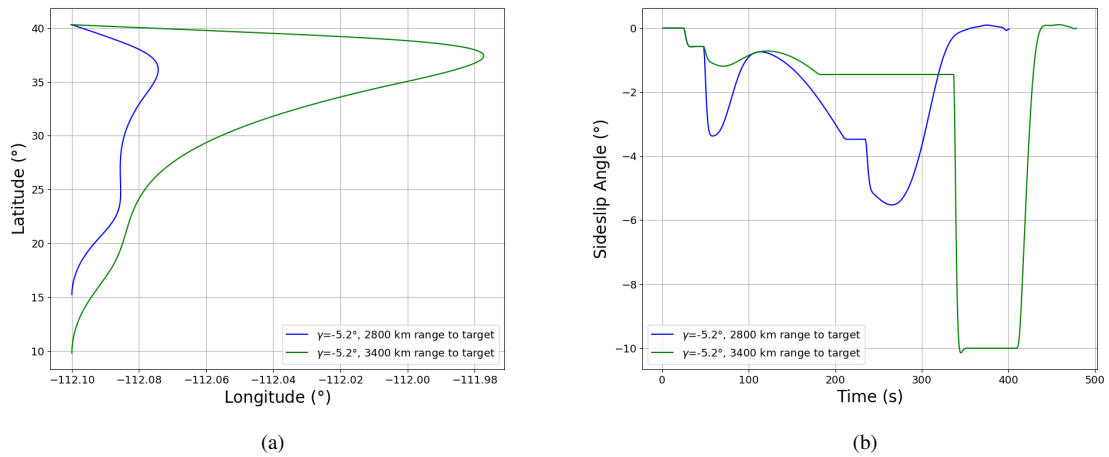


Figure 11 Baseline Selection Effect on Incurred Crossrange: a) Groundtrack; b) Sideslip

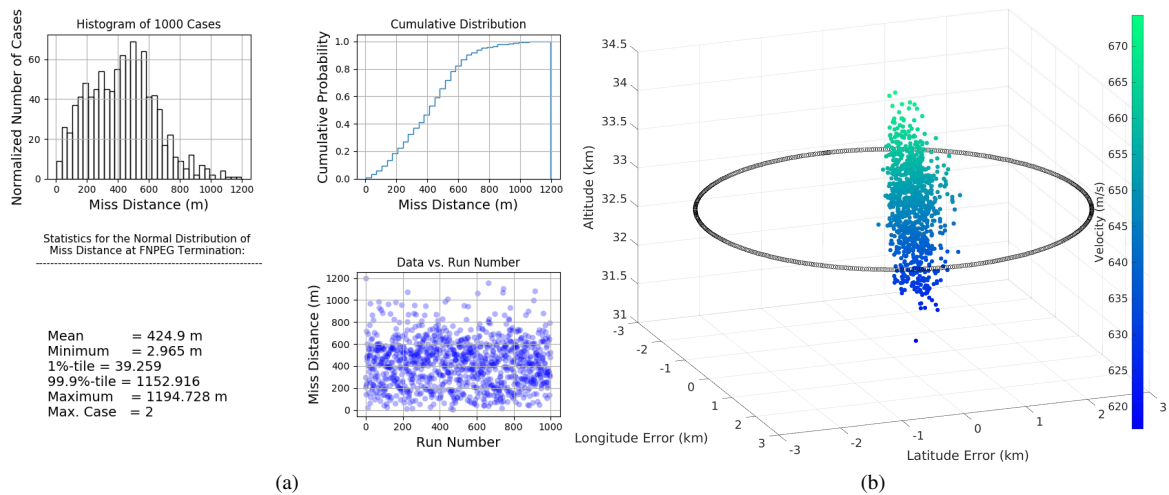


Figure 12 FNPEG URC Baseline Miss Distance Performance for 1,000-run Monte Carlo: a) Statistics; b) Energy States at Target (3km radius circle)

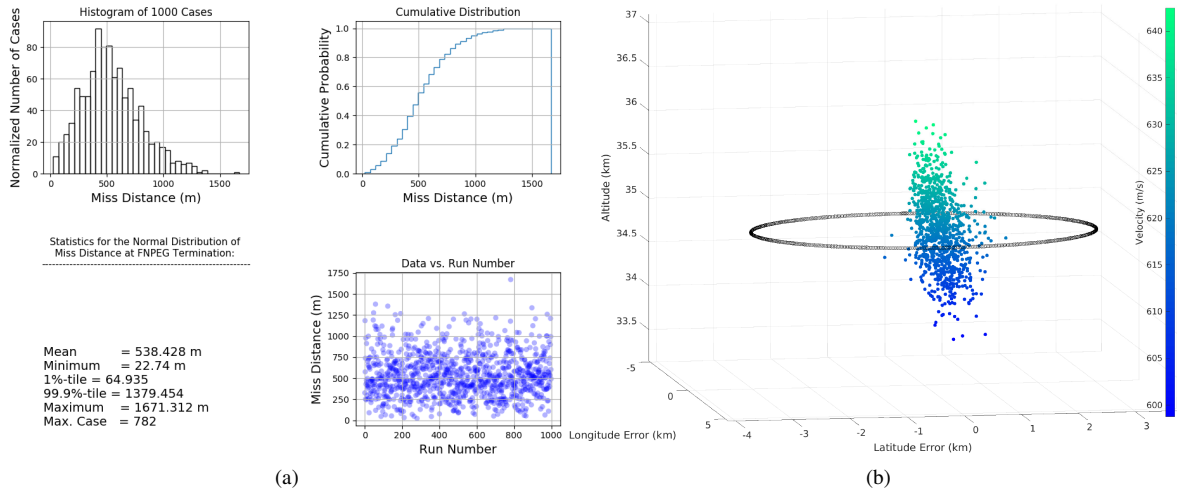


Figure 13 FNPEG Comparison to FNPEG URC Baseline Miss Distance Performance for 1,000-run Monte Carlo: a) Statistics; b) Energy States at Target (3km radius circle)

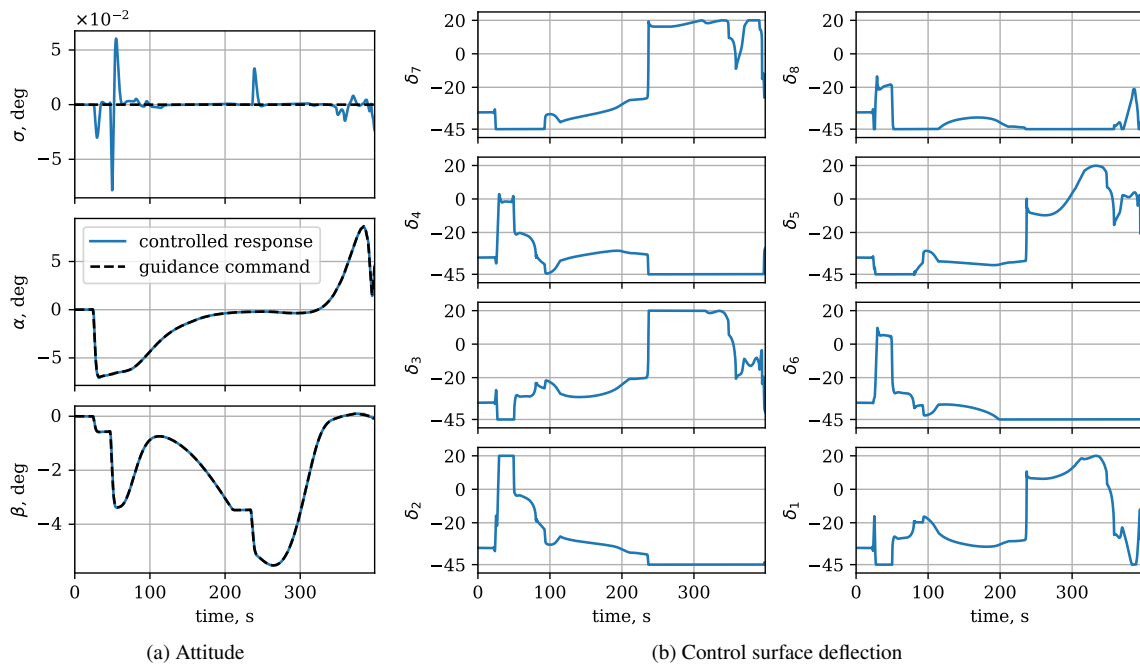


Figure 14 Simulation results for angle of attack and sideslip tracking during entry

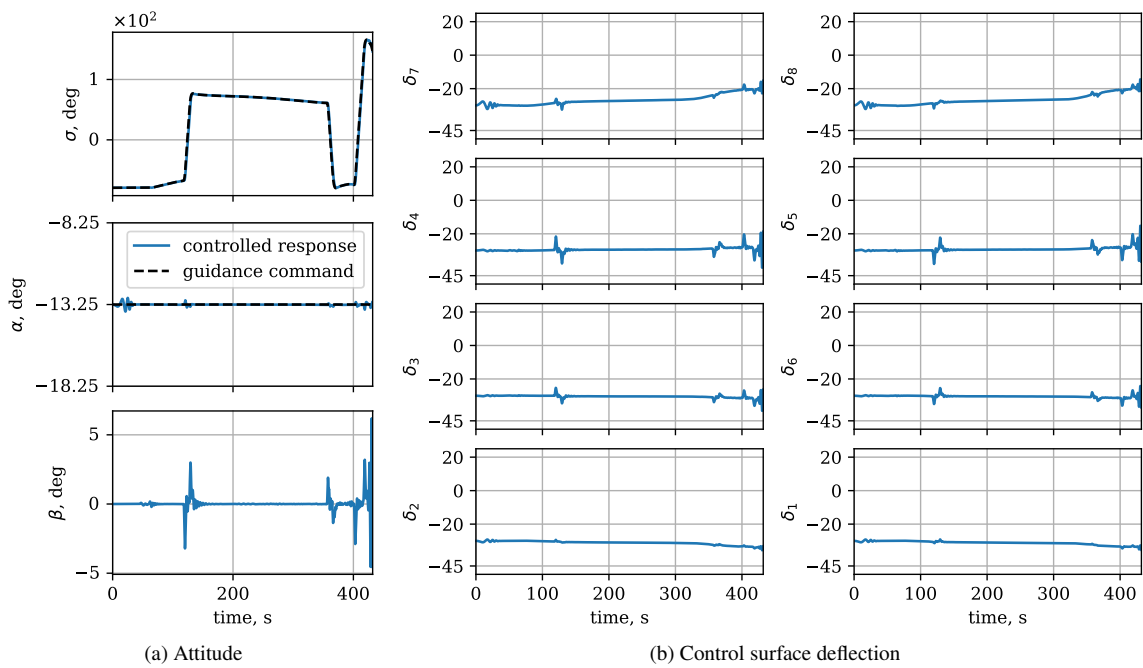


Figure 15 Simulation results for bank angle tracking during entry